ACS OMEGA

http://pubs.acs.org/journal/acsodf

Article

Microwave-Assisted Coprecipitation Synthesis and Local Structural Investigation on NiO, β-$Ni(OH)_2/Co_3O_4$ Nanosheets, and Co_3O_4 Nanorods Using X-ray Absorption Spectroscopy at Co−Ni K-edge and Synchrotron X-ray Diffraction

Umesh P. Gawai,* Shilpa D. Kamble, Sanjay K. Gurav, Manvendra N. Singh, Ashok K. Yadav, Shambhu N. Jha, Niranjan P. Lalla, Milind R. Bodke, Mahendra D. Shirsat, and Babasaheb N. Dole

Cite This: *ACS Omega* 2022, 7, 6700−6709

Read Online

ACCESS | Metrics & More | Article Recommendations

ABSTRACT: Developing the most straightforward, cheapest, and eco-friendly approaches for synthesizing nanostructures with well-defined morphology having the highest possible surface area to volume ratio is challenging for design and process. In the present work, nanosheets of NiO and β-$Ni(OH)_2/Co_3O_4$, and nanorods of Co_3O_4 have been synthesized at a large scale via the microwave-assisted chemical coprecipitation method under low temperature and atmospheric pressure. X-ray absorption spectroscopy (XAS) measurements, which comprises both X-ray absorption near-edge structure (XANES) and extended X-ray absorption fine structure (EXAFS) techniques, have been carried out at Co and Ni K-edges to probe the electronic structure of the samples. Also, the local atomic structural, chemical bonding, morphological, and optical properties of the sample were systematically investigated using XAS, synchrotron X-ray diffraction (SXRD), Raman spectroscopy, FTIR, transmission electron microscopy (TEM), and UV−visible spectroscopy. The normalized XANES spectra of the β-$Ni(OH)_2/Co_3O_4$ nanosheets show the presence of Ni^{2+} and a mixed oxidation state of Co. The disorder factor decreases from β-$Ni(OH)_2/Co_3O_4$ to Co_3O_4 with increasing Co−O bond length. The SXRD pattern analyzed using Rietveld refinement reveals that NiO has a face-centered cubic phase, Co_3O_4 has the standard spinal structure, and β-$Ni(OH)_2/Co_3O_4$ has a mixed phase of hexagonal and cubic structures. TEM images revealed the formation of nanosheets for NiO and β-$Ni(OH)_2/Co_3O_4$ samples and nanorods for Co_3O_4 samples. FTIR and Raman spectra show the formation of β-$Ni(OH)_2/Co_3O_4$, which reveals the fingerprints of Ni−O and Co−O.

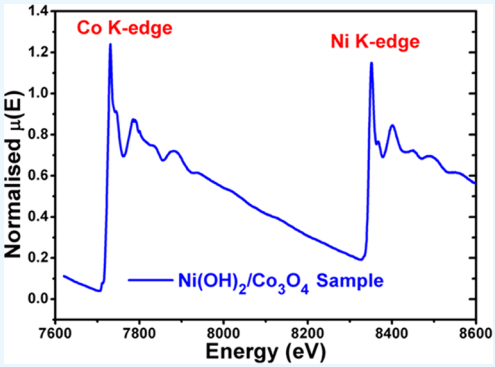

INTRODUCTION

The shape, size, and surface area of metal oxides at the nanoscale have a significant impact on their structural, electrical, chemical, and catalytic properties. Exploring low-cost and eco-friendly approaches to inculcate the development of metal oxide nanomaterials for desired structures and well-defined facets would be a significant step in the progress and development of research and industrial applications.[1] The method presented here to develop nanosheets and nanorods by simple microwave-assisted chemical coprecipitation methods may be one of the promising approaches. Nowadays, various nanomaterials have been studied due to their unique properties at the nanoscale compared to the bulk materials. Among them, two-dimensional (2D) nanomaterials like graphene and inorganic nanosheets have been receiving great attention due to their fascinating physical and chemical properties for various applications.[2,3] This great importance of 2D nanomaterials in catalysis[4,5] and energy devices is due to their fewer ion/electron diffusion path distance, significant electrochemical activity, high electronic conductivity, and improved structural stability. They can also provide surface-dependent electrochemical performance for next-generation batteries and supercapacitor applications.[6,7]

In particular, a high interest in the preparation of transition metal−metal oxide heterojunction 1D and 2D nanomaterials such as nickel oxide/cobalt oxide (NiO/Co_3O_4), nickel/nickel oxide (Ni/NiO), nickel hydroxide/cobalt oxide ($Ni(OH)_2/Co_3O_4$), and α-$Ni(OH)_2$ has been seen for their applications in supercapacitors,[8,9] solar cells,[10] ferro-fluids, catalysis,[11] magnetic materials,[12] gas sensors,[13,14] and as efficient anodes in lithium batteries.[15] It is well known that CoO occurs in 6

Received: November 3, 2021
Accepted: January 17, 2022
Published: February 14, 2022

ACS Publications

© 2022 The Authors. Published by American Chemical Society

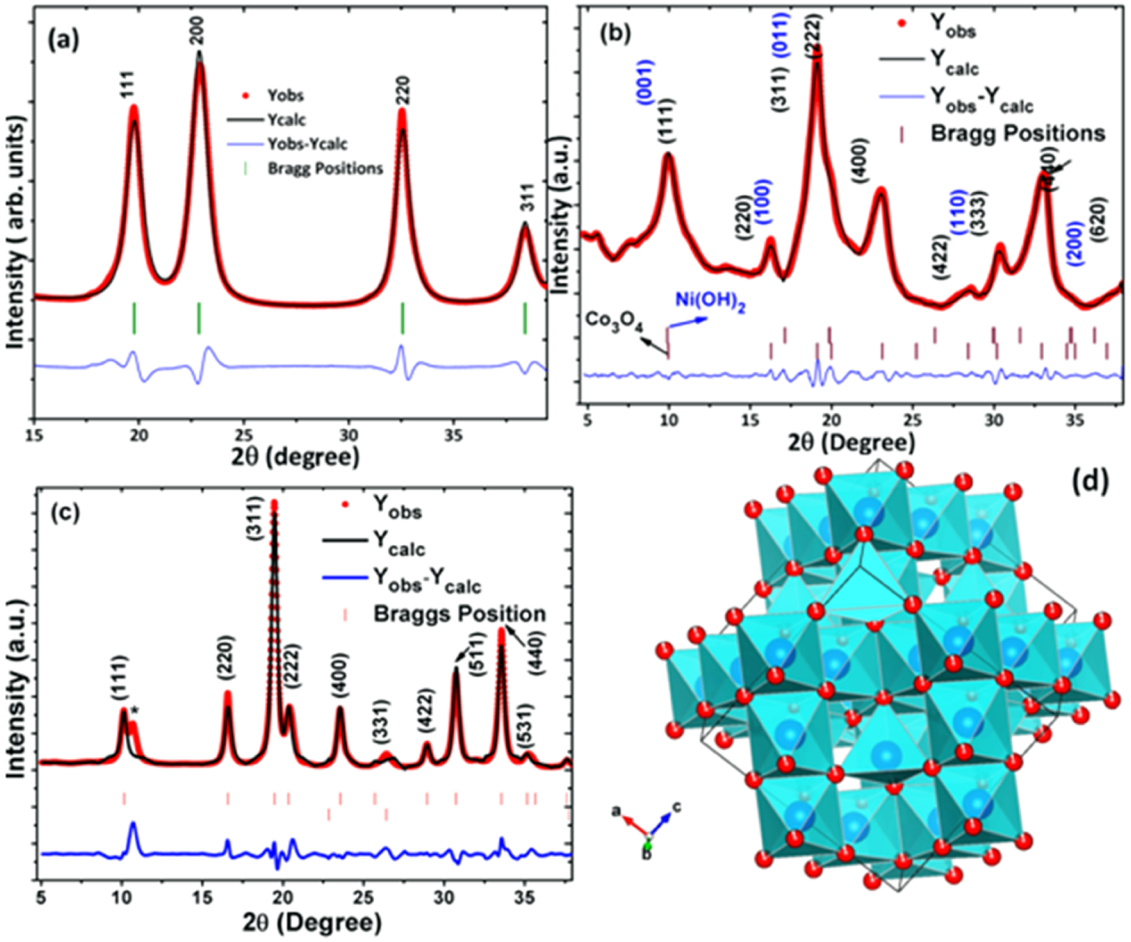

Figure 1. (a–c) SXRD patterns of samples of NiO, β-Ni(OH)$_2$/Co$_3$O$_4$ nanosheets, and Co$_3$O$_4$ nanorods; (d) cubic structure of the Co$_3$O$_4$ sample.

different oxidation states, such as Co, CoO_2, Co_2O_3, CoO(OH), CoO, and Co_3O_4.[16,17] Nickel hydroxide Ni(OH)$_2$ has received great attention due to its high theoretical capacitance for supercapacitor applications and high performance in battery applications.[18−24] NiO and Co_3O_4 are p-type antiferromagnetic semiconductors with direct band-gap energy in the range of 3.6−4.3 eV.[23] The structure of NiO is similar to that of NaCl, with octahedral Ni^{2+} and O^{2-} sites having face-centered cubic (fcc) structure (rock salt structure), whereas Ni has a hexagonal hcp and fcc structure. The stoichiometric ratio (1:1) of NiO shows a green color, and non-stoichiometric NiO appears black.[23,24] There are many methods available for the synthesis of 1D and 2D nanomaterials; among them, microwave synthesis methods are very fast. Tian et al.[21] and Bazgir et al.[22] report on the microwave synthesis of nanoball-like mesoporous α-Ni(OH)$_2$ as a precursor for NiO_x for supercapacitor applications and Co_3O_4 nanorods for photocatalytic degradation of methylene blue under visible light irradiation, respectively. A variety of high-cost methods are involved in the synthesis of morphologically essential nanomaterials.[25]

In this report, a simple microwave-assisted chemical coprecipitation method was implemented to synthesize NiO, β-Ni(OH)$_2$/Co$_3$O$_4$ nanosheets, and Co$_3$O$_4$ nanorod samples. Herein, β-Ni(OH)$_2$/Co$_3$O$_4$ nanosheets were synthesized with a 1:1 molar ratio of nickel nitrate and cobalt nitrate chemicals. For an in-depth investigation of the local structural study of samples by as-synthesis, we combined XAS and SXRD patterns. XAS is the combination of X-ray near-edge structure (XANES) and extended X-ray absorption fine structure (EXAFS). XANES is used to investigate charge transfer, orbital occupancy, and symmetry. The Fourier transform of EXAFS was used to obtain the bond length, and coordination details were extracted from the synthesized samples. The elemental specific nature and high sensitivity of the local chemical structure of the XAS technique make it an ideal tool to investigate the electronic structural properties and interatomic environment.[26] Rietveld refinement of the synchrotron X-ray diffraction data reflects the formation of NiO with face-centered cubic phase, Co$_3$O$_4$ with spinal cubic phase, and β-Ni(OH)$_2$/Co$_3$O$_4$ with hexagonal and spinal cubic mixed phases. Again, the structural and morphological properties were investigated by TEM using SAED patterns of the as-synthesized samples.

RESULTS AND DISCUSSION

Crystallographic Study. The synchrotron X-ray diffraction patterns shown in Figure 1 were used to obtain the detailed crystallography of the as-synthesized samples. Structural analysis of samples from SXRD data and Rietveld refinement was carried out using FULLPROF software.[2,30,31] Figure 1a–c displays the SXRD patterns of samples of NiO, Ni(OH)$_2$/Co$_3$O$_4$ nanosheets, and Co$_3$O$_4$ nanorods, where the red, black, and blue curves indicate the observed pattern, calculated pattern, and the difference between the observed and calculated pattern, respectively. In the SXRD patterns of

https://doi.org/10.1021/acsomega.1c06179
ACS Omega 2022, 7, 6700−6709

Figure 1a NiO exhibits sharp peak reflections at positions 2θ = 19.78, 22.90, 32.49, and 38.43, which can be readily indexed to (111), (200), (220), and (311), respectively. These reflections can be indexed as a face-centered cubic (fcc) structure with space group $Fm\bar{3}m$ for cubic NiO (JCPDS card no. 03-065-2901) at lattice parameter a = 4.19420 ± 0.044 Å without any trace of additional impurity. The obtained lattice parameters from the SXRD data of the NiO nanosheets are well in agreement with the reported literature.[10] Figure 1b shows the diffraction pattern of the β-$Ni(OH)_2/Co_3O_4$ sample. Figure 1b shows five diffraction peaks (blue color) at angles 2θ = 9.90, 17.14, 19.48, 27.11, and 34.69 in the SXRD pattern, which can, respectively, be assigned to the (001), (100), (011), (110), (012), and (200) reflection indexes of β-$Ni(OH)_2$. The refined lattice parameters for the $Ni(OH)_2/Co_3O_4$ sample are found to be a = 3.1506 ± 0.038 Å and c = 4.7123 ± 0.0541Å (JCPDS no. 14-0117), and β-$Ni(OH)_2$ crystallized as a hexagonal structure with a space group of (164) $P\bar{3}m1$ of the β-$Ni(OH)_2/Co_3O_4$ sample. The other nine diffraction peaks from Figure 1b can be attributed to the Co_3O_4 phase at 9.95, 16.59, 19.13, 19.98, 23.12, 28.41, 30.17, 32.92, and 36.94, indexed by (111), (220), (311), (222), (400), (422), (333), (440), and (620) for the cubic spinel structure of space group (277) $Fd\bar{3}m$ (JCPDS no. 43-1003) at the lattice parameter a = 8.1195 ± 0.14 Å.[32,33] The lattice constants calculated from the SXRD data of the NiO nanosheets are well in agreement with the reported data.[9] Also, the diffraction patterns of the Co_3O_4 sample given in Figure 1c evidence the cubic spinel phase of the samples with space group (277) $Fd\bar{3}$m at the reflection indexes of (111), (220), (311), (222), (400), (331), (422), (511), (440), and (531), respectively, for angles 2θ = 10.14, 16.29, 19.48, 2.36, 23.55, 25.70, 28.94, 30.74, 33.55, and 35.13 for a lattice constant a = 8.0868 Å (JCPDS no. 43-1003).[33] An additional minute peak (indicated by the star) appears in the Co_3O_4 sample's SXRD as shown in Figure 1c, which is due to the splitting of the (111) peak.

Gaussian function fitting[34] was used to find out the full width at half-maximum ($fwhm$) values from the diffraction peaks of the samples. The average crystallite size was estimated from the Scherrer formula $D = k\lambda/\beta \cos\theta$, where β is the $fwhm$ of the diffraction peak, k is the Scherrer constant (0.94), θ is the diffraction angle, and λ is the incident X-ray wavelength (0.82521 Å). It is found that the average crystallite sizes of NiO, β-$Ni(OH)_2/Co_3O_4$ nanosheets, and Co_3O_4 nanorods are 5.5 ± 0.87, 3.42 ± 0.33, and 11.22 ± 1.07 nm, respectively. The SXRD results are in accordance with the TEM and SAED patterns.

X-ray Absorption Spectroscopic Study. The X-ray absorption spectroscopy (XAS) measurements, which comprise both X-ray near-edge structure (XANES) and extended X-ray absorption fine structure (EXAFS) techniques, were carried out on Co and Ni K edges to probe the local structure. The XAS measurements were carried out at the Energy-Scanning EXAFS beamline (BL-9) at the Indus-2at RRCAT, Indore, India.[33,34]

The normalized XANES spectra at the Ni K-edge and Co K-edge are shown in Figures 2 and 3, respectively. They provide detailed information about the oxidation state and coordination environment of the Ni and Co atoms. The position of the absorption edge depends on the oxidation state of the absorbing atom. From Figure 2, the Ni-edge[35,36] positions of NiO and β-$Ni(OH)_2/Co_3O_4$ nanosheets are found to be at the same energy, indicating +2 oxidations for both the samples.

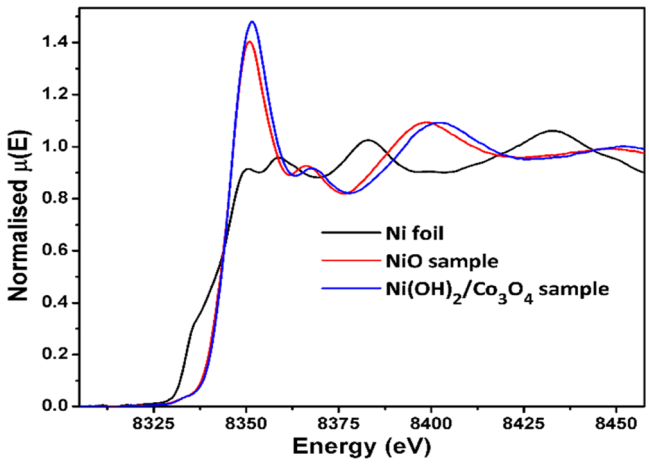

Figure 2. Normalised XANES spectra at Ni K-edge along with standard samples.

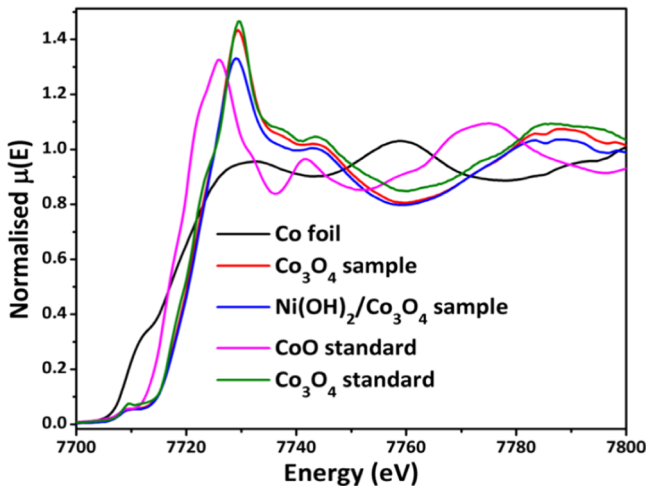

Figure 3. Normalized XANES spectra at the Co K-edge along with standard samples.

There is no significant change observed between NiO and β-$Ni(OH)_2/Co_3O_4$ nanosheets except for a small increase in the white -line peak intensity (8351 eV) of β-$Ni(OH)_2/Co_3O_4$ and a phase shift in EXAFS oscillations. This indicates a small alteration in the structure of β-$Ni(OH)_2/Co_3O_4$ compared to NiO. The normalized XANES spectrum at the Co K-edge is shown in Figure 3 along with CoO and Co_3O_4 standards. The absorption edge position and XANES profile of Co_3O_4 and β-$Ni(OH)_2/Co_3O_4$ samples match with those of the Co_3O_4 standard or bulk material, clearly indicating that the local electronic structure of Co_3O_4 is present in these two samples. In Figure 3, the normalized XANES spectra of the Co K-edge energy indicate the oxidation state of cobalt ions in +2 to +3, with a slight change in intensity from Co_3O_4 to β-$Ni(OH)_2/Co_3O_4$ samples, whereas Figure 4 represents the presence of Co-edge and Ni-edge in the β-$Ni(OH)_2/Co_3O_4$ samples. This is also corroborated by the EXAFS analysis part below. There is a small decrease in the white-line peak intensity (7729 eV) observed for β-$Ni(OH)_2/Co_3O_4$ compared to the Co_3O_4 sample.

The local structure around the absorbing atom is obtained from the quantitative analysis of the EXAFS spectra.[37,38] In order to take care of the oscillations (Figures 5 and 6) in the absorption spectra, $\mu(E)$ was converted to the absorption

https://doi.org/10.1021/acsomega.1c06179
ACS Omega 2022, 7, 6700−6709

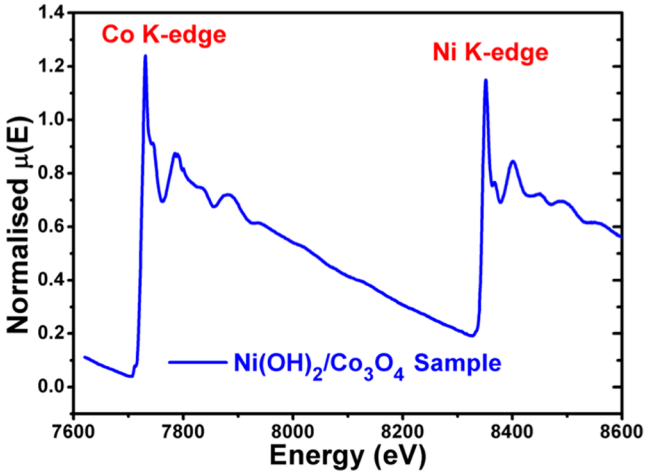

Figure 4. Normalized XANES spectra of β-$Ni(OH)_2/Co_3O_4$ samples at the Co K-edge and Ni-edge.

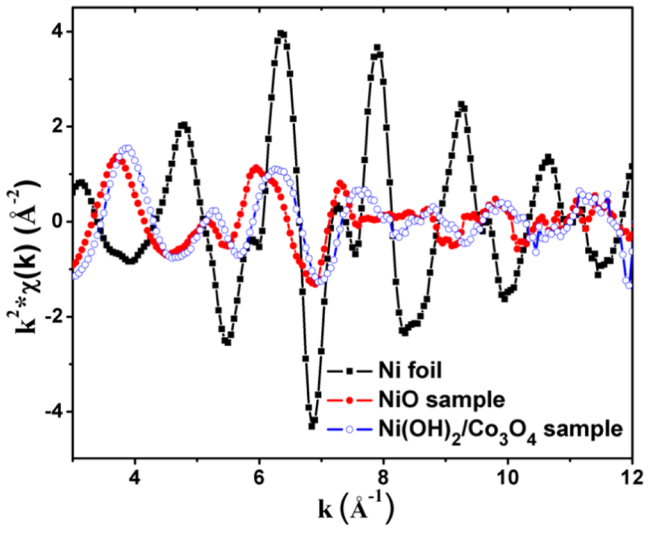

Figure 5. EXAFS oscillation obtained after background subtraction at the Ni K-edge.

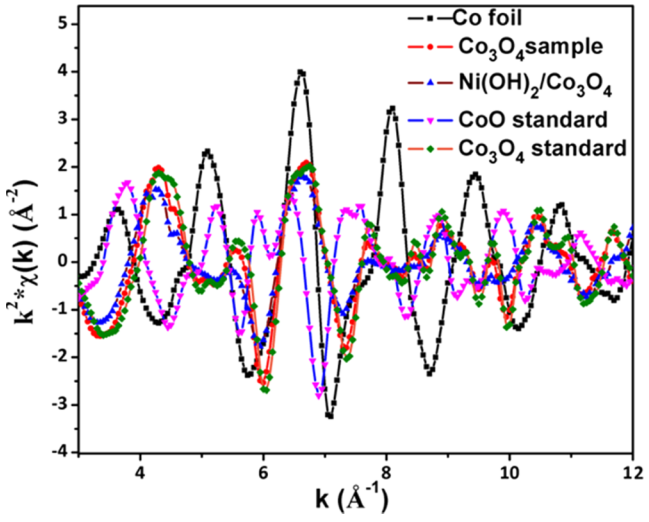

Figure 6. EXAFS oscillation obtained after background subtraction at the Co K-edge.

function $\chi(E)$. The set of EXAFS data analysis programs available within the Demeter software package have been used for EXAFS data analysis.[38] This includes background reduction and Fourier transform to derive the $\chi(R)$ versus R plots from the absorption spectra (using ATHENA software), generation of the theoretical EXAFS spectra starting from an assumed crystallographic structure, and finally, fitting of the experimental data with the theoretical spectra using ARTEMIS software.

The $\chi(R)$ versus R plots generated using Fourier transform of $\chi(E)$ versus E spectra by following the methodology described above are shown in Figure 7 at the Ni K-edge and

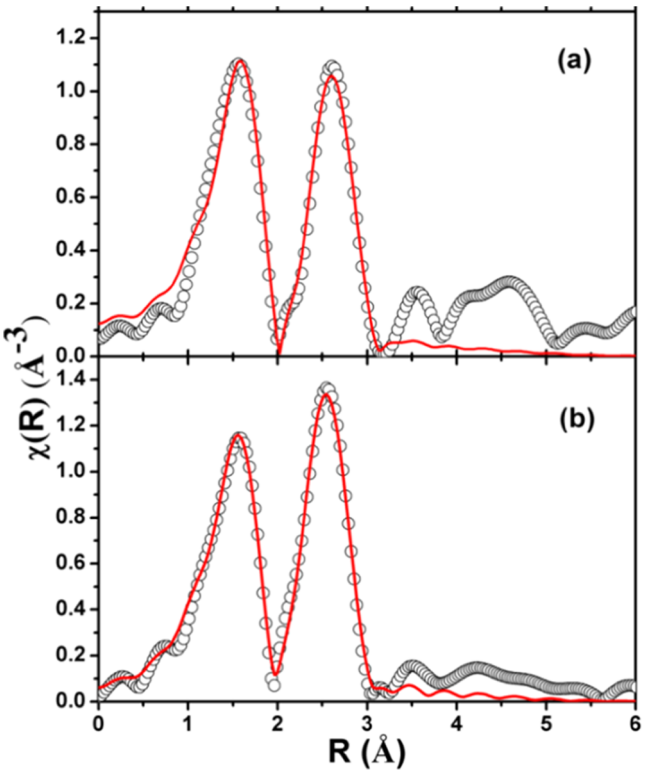

Figure 7. (a) Fourier-transformed EXAFS spectra of the NiO sample and (b) β-$Ni(OH)_2/Co_3O_4$ sample at the Ni K-edge along with the best fit. The experimental spectra are represented by scatter points, and the theoretical fits are represented by the solid line.

Figure 8c,d at the Co K-edge. The initially guessed structure of NiO is used for Ni K-edge fitting to generate theoretical scattering paths. The Fourier transform spectrum of NiO and β-$Ni(OH)_2/Co_3O_4$ samples shows two strong coordination peaks (Figure 7) at ~1.56 and ~2.60 Å, respectively. Note that the Fourier transform spectrum shown here is not phase corrected; hence, the coordination peaks will appear at the slightly lower R side compared to the actual bond lengths. The first peak is fitted with the Ni−O coordination path, and the second peak is fitted with the Ni−Ni coordination path. The bond distances, coordination numbers, and Debye−Waller factors (σ^2), which give the mean square fluctuations in the distances, and their best fitted results are shown in Tables 1 and 2 for Ni K-edge and Co K-edge measurements. The β-$Ni(OH)_2/Co_3O_4$ sample shows a small decrease in Ni−O bond length (0.03 Å) and Ni−Ni bond length (0.07 Å) with a small increase in the coordination number. We can also see the decrease in the Fourier transform spectrum intensity in the

https://doi.org/10.1021/acsomega.1c06179
ACS Omega 2022, 7, 6700−6709

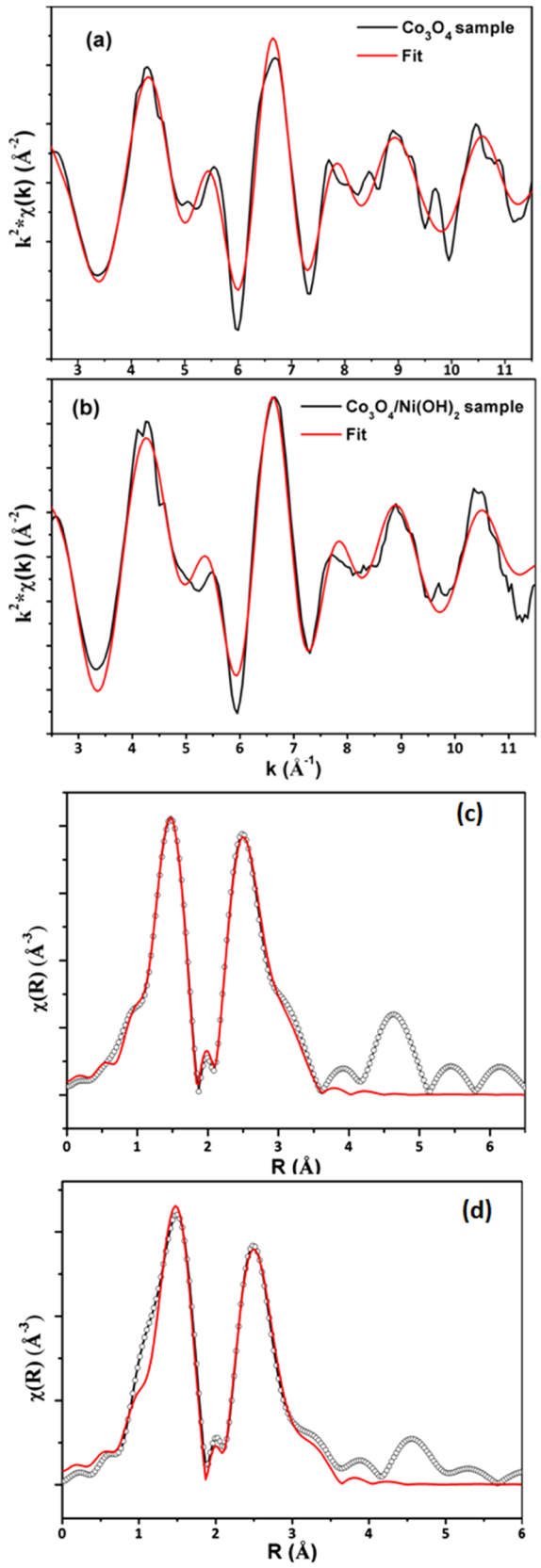

Figure 8. EXAFS oscillation and fit of the (a) Co_3O_4 sample, (b) β-Ni(OH)$_2$/Co_3O_4 sample, and the corresponding Fourier-transformed EXAFS spectra of the (c) Co_3O_4 sample and (d) β-Ni(OH)$_2$/Co_3O_4 sample at the Co K-edge along with the best fit. The experimental spectra are represented by Scatter points and the theoretical fits are represented by the solid line.

Table 1. Bond Length, Coordination Number, and Disorder Factor Obtained by EXAFS fitting at the Ni K-Edge

path	parameter	NiO	β-Ni(OH)$_2$/Co_3O_4
Ni-O	R (Å)	2.068 ± 0.009	2.036 ± 0.006
	N	5.5 ± 0.4	5.3 ± 0.3
	σ^2	0.0069 ± 0.0015	0.0081 ± 0.0011
Ni-Ni	R (Å)	3.033 ± 0.009	2.962 ± 0.005
	N	11.1 ± 0.8	11.5 ± 0.5
	σ^2	0.0146 ± 0.0013	0.0133 ± 0.0007

Table 2. Bond Length, Coordination Number, and Disorder Factor Obtained by EXAFS Fitting at the Co K-Edge[a]

path	parameter	Co_3O_4	β-Ni(OH)$_2$/Co_3O_4
Co-O	R (Å)	1.90 ± 0.01	1.91 ± 0.01
	N	5.28 ± 0.36	4.56 ± 0.42
	σ^2	0.0018 ± 0.0009	0.0024 ± 0.0014
Co-Co	R (Å)	2.85 ± 0.02	2.88 ± 0.02
	N	5.28 ± 0.92	5.84 ± 1.21
	σ^2	0.0052 ± 0.0017	0.0079 ± 0.0025
Co-Co	R (Å)	3.35 ± 0.02	3.37 ± 0.02
	N	11.28 ± 0.42	4.64 ± 0.43
	σ^2	0.0112 ± 0.0028	0.0097 ± 0.0067

[a]The parameter is kept fixed.

region of 3−5 Å (Figure 7) for β-Ni(OH)$_2$/Co_3O_4 compared to NiO. Figure 8c,d shows the Fourier transform EXAFS spectrum at the Co K-edge. Figure 8a,b shows EXAFS fits with k-space fitting and also shows two coordination peaks at ∼1.47 and ∼2.48 Å. The first peak at ∼1.47 Å is fitted with the bond length of ∼1.88 Å, which is much lower than the Co−O bond length (∼2.04 Å). Then we compared the CoO and Co_3O_4 commercial standards with Co EXAFS data (Figure 9) and found that it exactly matches with the Co_3O_4 nanorod sample, which is also corroborating the XANES observation discussed above. We used the Co_3O_4 structure to fit the EXAF spectrum of Co_3O_4 and β-Ni(OH)$_2$/Co_3O_4 at the Co K-edge, and the fitting results are shown in Table 2. There are two equivalent sites (tetrahedral and octahedral) in Co_3O_4. However, because of the existing data range, which limits the maximum number of independent parameters that can be varied during the fitting, we carried out fitting using three paths only and varied their bond length, coordination number, and disorder factor. The results obtained from the XAS study of the Ni and Co K-edge is well in agreement with the reported literature.[12,39]

Morphological Investigation. Figure 10 shows the transmission electron microscopy (TEM) micrograph of NiO, β-Ni(OH)$_2$/Co_3O_4 nanosheets, and Co_3O_4 nanorod samples. In particular, TEM micrographs of Figure 10a,b and d,e reveal the formation of nanosheets of NiO and β-Ni(OH)$_2$/Co_3O_4, and those of Figure 10g,h reveal the formation of nanorods of Co_3O_4. These formations have taken place by the simple microwave-assisted chemical coprecipitation method. The thicknesses of NiO, β-Ni(OH)$_2$/Co_3O_4 nanosheets, and Co_3O_4 nanorods are found to be ∼7.6, ∼3.5, and ∼33 nm, respectively. The nanorods' lengths, as evaluated from the TEM micrographs of Co_3O_4, are found to be ∼283 nm. The d-spacing measured using SAEDs matches well with the d-spacing of SXRD analysis. Figure 10c,f shows a typical SAED pattern corresponding to the NiO and β-Ni(OH)$_2$/Co_3O_4 nanosheets consisting of three distinct concentric spotty rings. The d-spacings of NiO nanosheets as

https://doi.org/10.1021/acsomega.1c06179
ACS Omega 2022, 7, 6700−6709

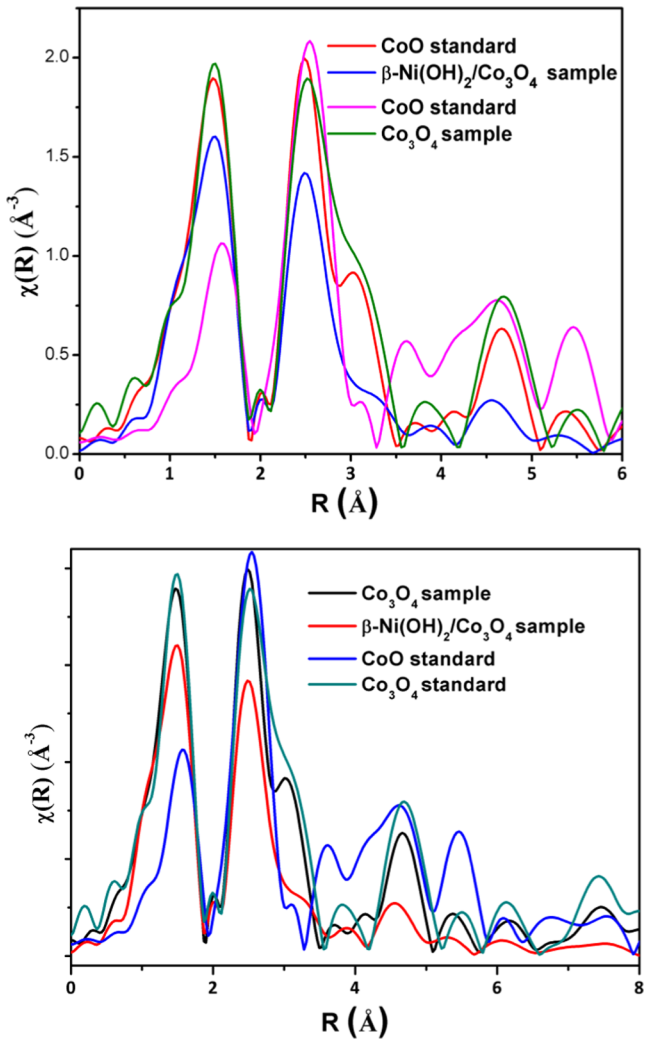

Figure 9. Fourier transformed EXAFS spectra of at the Co K-edge along with CoO and Co_3O_4 standards.

measured from the SAED pattern in Figure 10c are 0.498, 0.326, 0.152, and 0.140 nm, and are indexed, respectively, to (111), (200), (220), and (311). Figure 10f reveals the SAED pattern of $Ni(OH)_2/Co_3O_4$; the corresponding rings for $Ni(OH)_2$ give d_{hkl} values of 0.4712 and 0.2361 nm, appearing from the (001) and (011) planes. The corresponding rings for Co_3O_4 for d_{hkl} values at 0.4787, 0.2343, 0.202, and 0.143 nm appear from planes (111), (222), (400), and (440), respectively. The Co_3O_4 nanorods also show the d_{hkl} values at 0.4687, 0.2343, 0.202, and 0.143 nm arising from (111), (222), (400), and (440), respectively. All of the SAED patterns show the mixed, polycrystalline, and textured nature of agglomeration. These obtained d_{hkl} values match well with the values measured using SXRD.

FTIR, Raman Shift, and UV−vis Spectroscopic Study. The FTIR spectra are given in Figure 11 for the as-synthesized samples. They were used to investigate the functional groups present in the samples and were recorded in the range of 400 to 4000 cm^{-1} at room temperature. The strong wide bands at 3336, 3353, and 3396 cm^{-1} indicate the O−H $\nu(H_2O)$ stretching vibration and that at ∼1624 cm^{-1} indicate the $\delta(H_2O)$ bending vibration characteristics of the water molecules for NiO, β-$Ni(OH)_2/Co_3O_4$ nanosheets, and Co_3O_4 nanorods, respectively. However, the peak at 521 cm^{-1} indicates Ni−O bonds in the fingerprint region for the NiO nanosheet sample.[40,41] The absorption bands at 527.7 and 642.3 were assigned to Co−O and Ni−O stretching vibration modes, indicating Co−O and Ni−O bonds in the fingerprint region for the β-$Ni(OH)_2/Co_3O_4$ nanosheets. For Co_3O_4 nanorods having sharp bands at 549.61 and 653.2 cm^{-1} are associated for O−Co and Co-O−Co lattice vibration, respectively. The results of FTIR matched well with the reported literature and also indicate the presence of Ni and Co lattices in the samples.[40−42]

The Raman spectra of NiO, Co_3O_4, and β-$Ni(OH)_2/Co_3O_4$ samples taken using 532 nm wavelength of visible LASER are shown in Figure 12. In Figure 12a, the Raman peaks of the NiO nanosheets at 492, 709, and 1044 cm^{-1} were assigned to the first-order longitudinal optical (LO) phonon modes, second-order transverse optical 2TO, and longitudinal optical 2LO phonon scattering of NiO, respectively.[24] Figure 12b shows the spectra of the synthesized Co_3O_4 sample with Co^{2+} ($3d^7$) and Co^{3+} ($3d^6$) situated at tetrahedral and octahedral sites, respectively. The Co_3O_4 sample crystallizes in cubic spinel structures of space group $Fd3m$ with symmetry $\Gamma = A_{1g}$ (R) + E_g (R) +F_{1g} (IN) + $3F_{2g}$ (R) + $2A_{2u}$ (IN) +2_{Eu} (IN) + $4F_{1u}$ (IR) + $2F_{2u}$ (IN), where R, IR, and IN represent Raman active vibrations, infrared-active vibrations, and inactive modes, respectively.[43,44] Figure 12b reveals the five active Raman modes at 180.2, 450.9, 494.7, 591, and 652 cm^{-1}, which are in agreement with the values of the pure Co_3O_4 spinel structure in the reported literature.[45] The band at 180 cm^{-1} (F_{2g}) exhibits CoO_6 vibration, and the other bands at 450.9, 494.7, 591, and 652 cm^{-1}correspond to E_g, $2F_{2g}$, and A_{1g}, which exhibit Co−O symmetric stretching vibration.[45,46]

Figure 12c displays Raman peaks at 177, 455, 502, 643, and 1050 cm^{-1} corresponding to the β-$Ni(OH)_2/Co_3O_4$ sample.[9] It can be observed that the Raman broad band between 450 and 519 cm^{-1} corresponds to the Ni−OH/Co−OH Ni−O/Co−O stretching modes, matching with the literature.[9,44−47] Hall et al.[44] reported on the β-$Ni(OH)_2$ A_{1g} mode of the O−H stretching at 1067 cm^{-1}; herein it is observed that the broadened peak at 1050 cm^{-1} in Figure 12c corresponds to the A_{1g} mode of the same O−H stretching of β-$Ni(OH)_2$ of the sample β-$Ni(OH)_2/Co_3O_4$.[9,44−46] The peak at 1050 cm^{-1} is also noted for the 2P mode of Ni−O.[47]

Figure 13a reflects the UV−Vis absorption spectra of the synthesized samples in the wavelength range of 200−900 nm. The strongest absorption peak is displayed at 249 and 330 nm for the NiO and β-$Ni(OH)_2/Co_3O_4$ sample, respectively, and three peaks appear at 226, 436, and 748 nm for the Co_3O_4 sample. These three distinct absorption band gaps at around 226, 436, and 748 nm are assigned to the charge transfer from O^{2-} to Co^{3+}, octahedral coordinated Co^{3+}, and transition of Co^{2+} in tetrahedral coordination in well-defined-order Co_3O_4 respectively.[48−50] Hence, the UV−vis result is consistent with Co_3O_4 as the phase assignment of the Raman spectra. The energy band gap of the samples was calculated by Tauc eq 1, with the plots displayed in Figure 13b.

$$\alpha h\nu = A(h\nu - E_g)^n \quad (1)$$

where h is Planck's constant, ν is the photon's frequency, E_g is the band gap, A is a constant, and n is a factor depending on the nature of the electron transition. $n = 1/2$ is used in eq 1 for direct allowed band gaps.[50] The energy band gap of bulk NiO, β-$Ni(OH)_2$, and Co_3O_4 is 4, 3.6, and less than 3 eV, respectively.[48−51] The energy band gap was estimated from

https://doi.org/10.1021/acsomega.1c06179
ACS Omega 2022, 7, 6700−6709

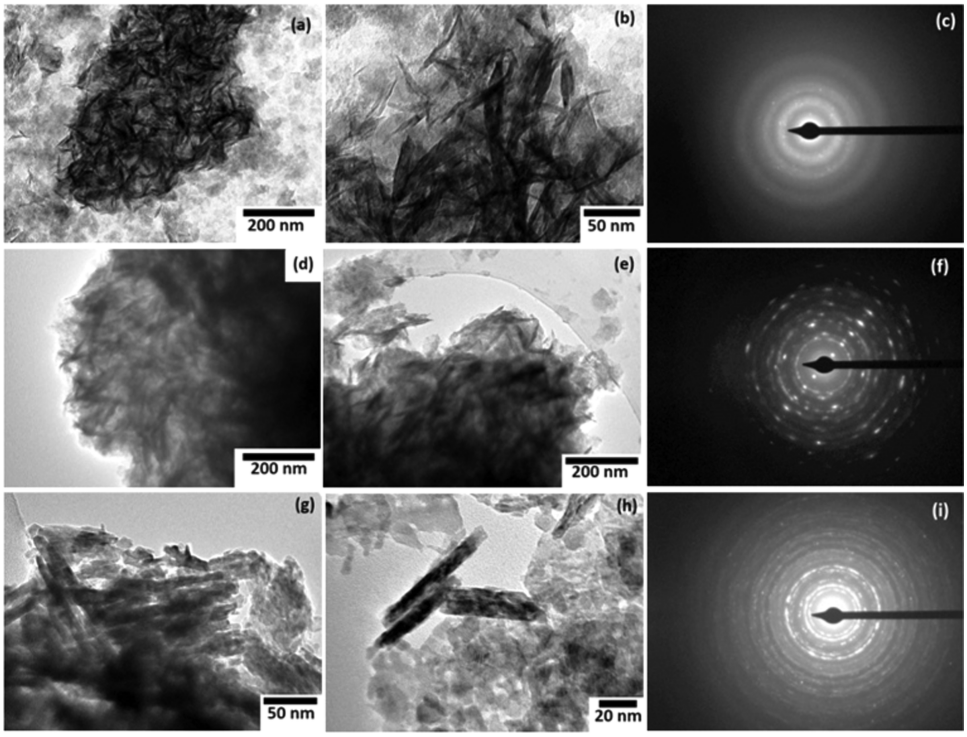

Figure 10. (a, b) and (d, e) show TEM micrographs of clusters of NiO and β-Ni(OH)$_2$/Co$_3$O$_4$ nanosheets, and the corresponding SAED patterns given in (c, f) show the mixed, polycrystalline, and textured nature of agglomeration, (g, h) show Co$_3$O$_4$ nanorods and (i) their SAED pattern. The nanorods are mostly randomly aggregated.

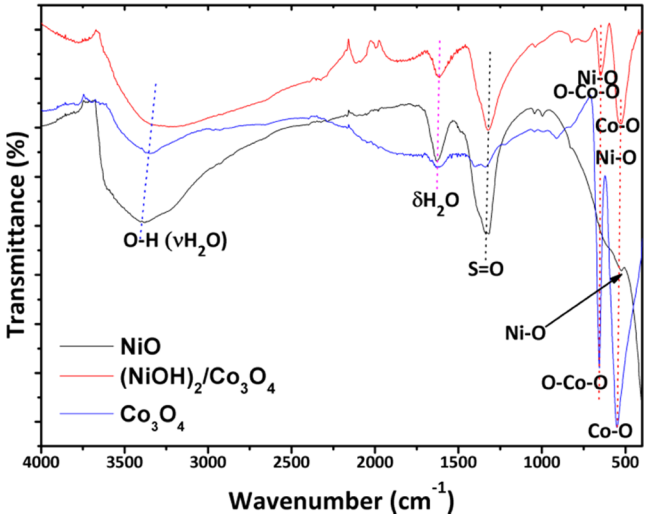

Figure 11. FTIR spectra of NiO, β-Ni(OH)$_2$/Co$_3$O$_4$ nanosheets, and Co$_3$O$_4$ nanorods.

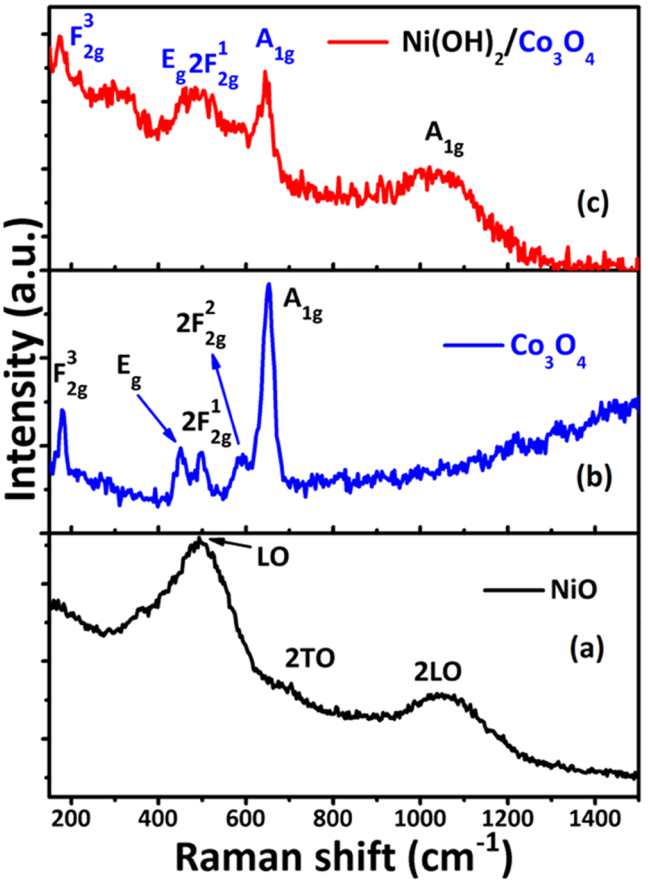

Figure 12. (a) Raman spectra of NiO, (b) β-Ni(OH)$_2$/Co$_3$O$_4$ nanosheets, and (c) Co$_3$O$_4$ nanorods.

Tauc plots, and it was found to be 2.29 and 3.6 eV for Co$_3$O$_4$ and 4.22 and 3.58 eV for β-Ni(OH)$_2$/Co$_3$O$_4$ and NiO samples, respectively, which is well in agreement with the reported literature.[48−53]

CONCLUSIONS

Samples of NiO, β-Ni(OH)$_2$/Co$_3$O$_4$, and Co$_3$O$_4$ were synthesized using the microwave-assisted chemical coprecipitation method. Local structure was evaluated from XAS and SXRD data. SXRD, TEM, and Raman shift were used to confirm the structure of the as-synthesized samples. The structural parameters were well matched with the Rietveld

https://doi.org/10.1021/acsomega.1c06179
ACS Omega 2022, 7, 6700−6709

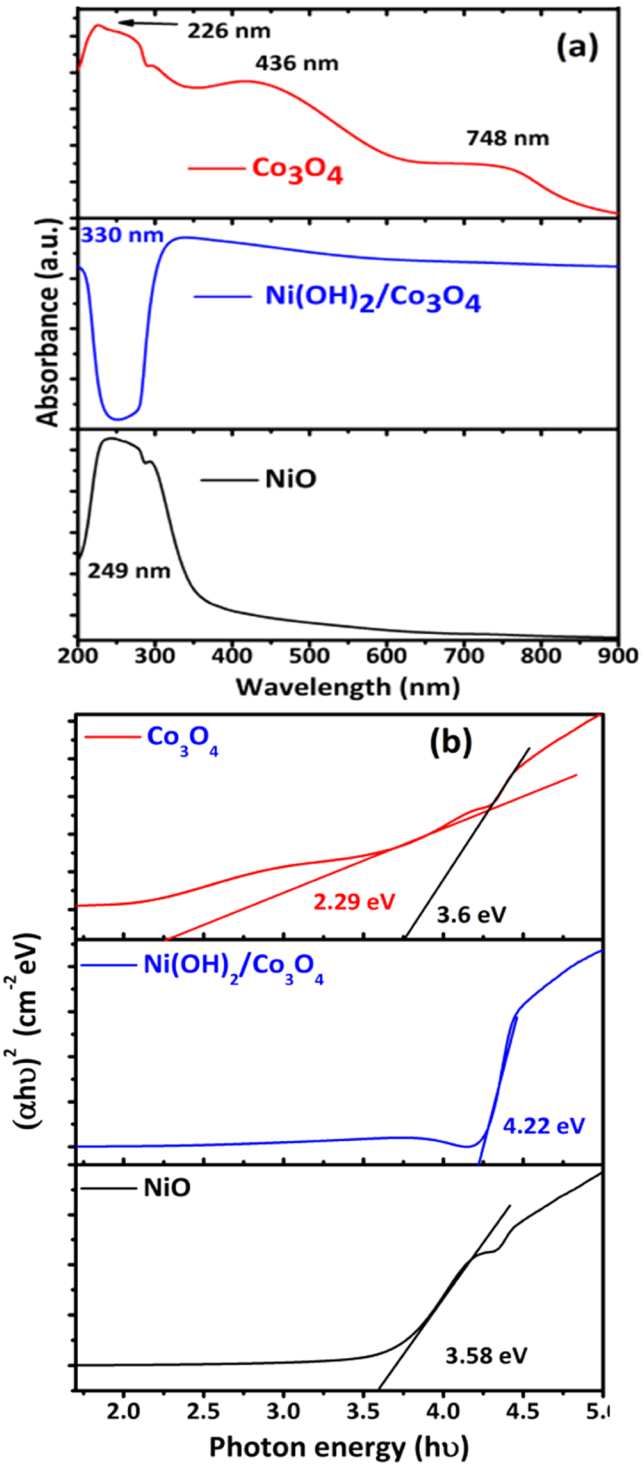

Figure 13. (a) UV−vis absorbance spectra and (b) Tauc's plot of NiO, $Ni(OH)_2/Co_3O_4$ nanosheets, and Co_3O_4 nanorods.

refinement of SXRD of the samples. It is confirmed from the SXRD patterns that the NiO, β-$Ni(OH)_2/Co_3O_4$, and Co_3O_4 samples were crystallized with fcc, hexagonal/cubic spinel, and cubic spinel structure, respectively. The TEM micrograph clearly reveals the formation of nanosheets of NiO, β-$Ni(OH)_2/Co_3O_4$, and Co_3O_4 nanorods. FTIR and Raman results show the Co−O, Ni−O, and O−H of β-$Ni(OH)_2$ vibration bands. The energy band gap of β-$Ni(OH)_2/Co_3O_4$ nanosheets is increased as compared to NiO and Co_3O_4 samples. The β-$Ni(OH)_2/Co_3O_4$ nanosheet sample shows different properties than the NiO and Co_3O_4 samples, which indicates its promising applications in the field of supercapacitors.

EXPERIMENTAL DETAILS

In the present work, the microwave-assisted chemical coprecipitation method has been implemented for the synthesis of NiO, β-$Ni(OH)_2/Co_3O_4$ nanosheets, and Co_3O_4 nanorods. For the synthesis of samples, analytical-grade nickel nitrate hexahydrate ($Ni(NO_3)_26H_2O$) and cobalt nitrate hexahydrate ($Co(NO_3)_26H_2O$), NaOH, and N,N-dimethylformamide (DMF) were used without any further purification. A typical reaction was carried out for NiO and Co_3O_4 as follows: the appropriate amount of nickel nitrate hexahydrate (1 mmol), cobalt nitrate hexahydrate (1 mmol), and NaOH (2 mmol) were dissolved separately with 50 mL of DMF and stirred for 1 h. For synthesis of β-$Ni(OH)_2/Co_3O_4$ nanosheets, the appropriate amount (1:1 ratio) of nickel nitrate hexahydrate (0.5 mmol), cobalt nitrate hexahydrate (0.5 mmol), and NaOH (1 mmol) were dissolved separately in beakers with 50 mL of DMF and stirred for 1 h. Then, NaOH solution was added to a mixture of precursors dropwise in all of the above-mentioned solutions; the beakers were placed inside a microwave oven for heating through microwave irradiation for 20 s for 5 cycles at 800 W output power and 2.45 GHz. After that, the solution was again stirred for 2 h at 40 °C till a clear precipitate was formed. The obtained precipitate was filtered, and washed with deionized water and ethanol several times. Finally, the obtained sample powder was dried at 100 °C overnight. Then, the obtained products were characterized.

CHARACTERIZATION OF THE SAMPLES

Synchrotron X-ray diffraction measurements were performed at Angle Dispersive X-ray Diffraction Beamline, BL-12, at INDUS-2 Raja Ramanna Centre for Advanced Technology (RRCAT), Indore, India.[27] This beamline is a bending magnet-based beamline and consists of an Si(111)-based double-crystal monochromator (DCM). The SXRD was recorded on the image plate area detector (MAR-345 dtb) experimental station in transmission mode using a monochromatic wavelength of 0.82521 Å. The sample to detector distance and the actual wavelength were accurately calibrated by measuring the SXRD of the LaB_6 NIST standard sample. Fit2D software was used to convert the image data into Intensity-2θ form. The XAS measurements (consisting of both X-ray absorption near-edge structure and extended X-ray absorption fine structure) of the as-synthesized samples were carried out at the Energy Scanning EXAFS beamline (BL-9 Indus-2 at source 2.5 GeV, 100 mA) in transmission mode at RRCAT, Indore, India. This beamline operates in the energy range of 4−25 KeV.[28,29] The beamline optics consists of an Rh/Pt-coated collimating meridional cylindrical mirror, and the collimated beam reflected by the mirror is monochromatized by a Si(111) ($2d$ = 6.2709 Å)-based double-crystal monochromator (DCM). The set of EXAFS data analysis software available within the IFEFFIT package was used for the EXAFS data analysis. This includes background reduction and Fourier transform to derive the w(R) versus R spectra from the absorption spectra (using ATHENA software), generation of the theoretical EXAFS spectra starting from an assumed crystallographic structure, and finally, fitting of the

https://doi.org/10.1021/acsomega.1c06179
ACS Omega 2022, 7, 6700−6709

experimental data with the theoretical spectra using ARTEMIS software. Transmission electron microscopy (TEM) images and selected-area electron diffraction (SAED) patterns of the samples were recorded at 200 kV accelerating voltage using TEM Tecnai-20 G2. Fourier transform infrared spectroscopy (FTIR, Bruker Tensor II), Raman shift (Horiba), and UV−vis (JASCOV-750) spectroscopic techniques were used for the optical study of the samples.

AUTHOR INFORMATION

Corresponding Author

Umesh P. Gawai − *Department of Physics, DDSP, Arts Commerce & Science College, Jalgaon 425 109 M.S., India;* orcid.org/0000-0003-3003-3973; Phone: +917219554819; Email: upgawai.phy@gmail.com

Authors

Shilpa D. Kamble − *Department of Physics, Shri Madhavrao Patil Mahavidyalaya, Osmanabad 413 606, India*

Sanjay K. Gurav − *Department of Physics, Shri Madhavrao Patil Mahavidyalaya, Osmanabad 413 606, India*

Manvendra N. Singh − *Synchrotrons Utilization Section, Raja Ramanna Centre for Advanced Technology, Indore 452 013, India*

Ashok K. Yadav − *Atomic & Molecular Physics Division, Bhabha Atomic Research Centre, Mumbai 400 094, India;* orcid.org/0000-0003-2716-0971

Shambhu N. Jha − *Beamline Development & Application Section, Bhabha Atomic Research Centre, Mumbai 400 094, India*

Niranjan P. Lalla − *UGC−DAE Consortium for Scientific Research, University Campus, Indore 452 001, India*

Milind R. Bodke − *Department of Electronics, Modern College of Arts, Commerce & Science, Pune 411 005 M.S., India*

Mahendra D. Shirsat − *Department of Physics & RUSA Centre for Advanced Sensor Technology, Dr. Babasaheb Ambedkar Marathwada University, Aurangabad 431 004 M.S., India*

Babasaheb N. Dole − *Department of Physics, Dr. Babasaheb Ambedkar Marathwada University, Aurangabad 431 004 M.S., India*

Complete contact information is available at: https://pubs.acs.org/10.1021/acsomega.1c06179

Author Contributions

The manuscript was written through the contributions of all authors.

Notes

The authors declare no competing financial interest.

ACKNOWLEDGMENTS

U.P.G. is thankful to D. Bhattacharyya, Atomic & Molecular Physics Division, Bhabha Atomic Research Centre, Mumbai 400 094, India, for availing the EXAFS beamline-9 of Raja Ramanna Centre for Advanced Technology, Indore. The author is also thankful to UGC-DAE, CSR Kolkata Centre, India, for providing financial assistance through Project UGC-DAE CSR-KC/CSR/19/MS01/0940.

ABBREVIATIONS USED

XAS, X-ray absorption spectroscopy; XANES, X-ray near edge structure; EXAES, extended X-ray absorption fine structure; SCXRD, synchrotron X-ray diffraction

REFERENCES

(1) Thomele, D.; Baumann, S.; Schneider, J.; Sternig, A.; Shulda, S.; Richards, R.; Schwab, T.; Zickler, G.; Bourret, G.; Diwald, O. Cubes to cubes: organization of MgO particles into one-Dimensional and two-Dimensional nanostructures. *Cryst. Growth Des.* **2021**, *21*, 4674−4682.

(2) Du, Y.; Yin, Z.; Zhu, J.; Huang, X.; Wu, X.; Zeng, Z.; Yan, Q.; Zhang, H. A general method for the large-scale synthesis of uniform ultrathin metal sulphide nanocrystals. *Nat. Commun.* **2012**, *3*, No. 1177.

(3) Sun, Y.; Sun, Z.; Gao, S.; Cheng, H.; Liu, Q.; Piao, J.; Yao, T.; Wu, C.; Hu, S.; Wei, S.; Xie, Y. Fabrication of flexible and freestanding Zinc chalcogenide single layers. *Nat. Commun* **2012**, *3*, No. 1057.

(4) Takagaki, A.; Takusagawa, C.; Hayashi, S.; Hara, M.; Domen, K. Nanosheets as highly active solid acid catalysts for green chemical syntheses. *Energy Environ. Sci.* **2010**, *3*, 82−93.

(5) Liu, J.; Liu, X. Two-Dimensional nanoarchitectures for Lithium storage. *Adv. Mater.* **2012**, *24*, 4097−4111.

(6) Zeng, Z.; Sun, T.; Zhu, J.; Huang, X.; Yin, Z.; Lu, G.; Fan, Z.; Yan, Q.; Hng, H.; Zhang, H. An effective method for the fabrication of few-layer-thick inorganic nanosheets. *Angew. Chem.* **2012**, *124*, 9186−9190.

(7) Guo, S.; Dong, S. Graphene nanosheet: synthesis, molecular engineering, thin film, hybrids, and energy and analytical applications. *Chem. Soc. Rev.* **2011**, *40*, No. 2644.

(8) Zhu, Y.; Cao, C.; Tao, S.; Chu, W.; Wu, Z.; Li, Y. Ultrathin Nickel Hydroxide and Oxide nanosheets: synthesis, characterizations and excellent supercapacitor performances. *Sci. Rep.* **2014**, *4*, No. 7091.

(9) Zhong, J.; Wang, A.; Li, G.; Wang, J.; Ou, Y.; Tong, Y. Co_3O_4/Ni(OH)2 composite mesoporous nanosheet networks as a promising electrode for supercapacitor applications. *J. Mater. Chem.* **2012**, *22*, No. 5656.

(10) Liu, Z.; Zhang, M.; Xu, X.; Cai, F.; Yuan, H.; Bu, L.; Li, W.; Zhu, A.; Zhao, Z.; Wang, M.; Cheng, Y.; He, H. NiO nanosheets as efficient top hole transporters for Carbon counter electrode based perovskite solar cells. *J. Mater. Chem. A.* **2015**, *3*, 24121−24127.

(11) Natile, M.; Glisenti, A. New NiO/Co_3O_4 and Fe_2O_3/Co_3O_4 nanocomposite catalysts: synthesis and characterization. *Chem. Mater.* **2003**, *15*, 2502−2510.

(12) Gawai, U.; Gaikwad, D.; Bodke, M.; Khawal, H.; Pandey, K.; Yadav, A.; Jha, S.; Bhattacharyya, D.; Dole, B. Doping effect on the local structure of metamagnetic Co doped Ni/NiO:GO core−shell nanoparticles using X-ray absorption spectroscopy and the pair distribution function. *Phys. Chem. Chem. Phys.* **2019**, *21*, 1294−1307.

(13) Qian, G.; Peng, Q.; Zou, D.; Wang, S.; Yan, B. Hydrothermal synthesis of flake-flower NiO and its gas sensing performance to CO. *Front. Mater.* **2020**, *7*, No. 216.

(14) Zhang, Z.; Wen, Z.; Ye, Z.; Zhu, L. Gas sensors based on ultrathin porous Co_3O_4 nanosheets to detect acetone at low temperature. *RSC Adv.* **2015**, *5*, 59976−59982.

(15) Zhang, Y.; Zhuo, Q.; Lv, X.; Ma, Y.; Zhong, J.; Sun, X. NiO-Co_3O_4 nanoplate composite as efficient anode in Li-ion battery. *Electrochim. Acta* **2015**, *178*, 590−596.

(16) Manickam, M.; Ponnuswamy, V.; Sankar, C.; Suresh, R. Cobalt oxide thin films prepared by nsp technique: impact of molar concentration on the structural, optical, morphological and electrical properties. *Optik* **2016**, *127*, 5278−5284.

(17) Yuan, C.; Hou, L.; Shen, L.; Li, D.; Zhang, F.; Fan, C.; Li, J.; Zhang, X. A novel method to synthesize whisker-like $Co(OH)_2$ and its electrochemical properties as an electrochemical capacitor electrode. *Electrochim. Acta* **2010**, *56*, 115−121.

https://doi.org/10.1021/acsomega.1c06179
ACS Omega 2022, 7, 6700−6709

(18) Li, H.; Yu, M.; Wang, F.; Liu, P.; Liang, Y.; Xiao, J.; Wang, C.; Tong, Y.; Yang, G. Amorphous Nickel Hydroxide nanospheres with ultrahigh capacitance and energy density as electrochemical pseudocapacitor materials. *Nat. Commun.* **2013**, *4*, No. 1894.
(19) Ji, J.; Zhang, L.; Ji, H.; Li, Y.; Zhao, X.; Bai, X.; Fan, X.; Zhang, F.; Ruoff, R. Nanoporous $Ni(OH)_2$ thin film on 3d ultrathin-graphite foam for asymmetric supercapacitor. *ACS Nano* **2013**, *7*, 6237−6243.
(20) Wang, R.; Lang, J.; Liu, Y.; Lin, Z.; Yan, X. Ultra-small, size-controlled $Ni(OH)_2$ nanoparticles: elucidating the relationship between particle size and electrochemical performance for advanced energy storage devices. *NPG Asia Mater.* **2015**, *7*, e183.
(21) Tian, X.; Cheng, C.; Qian, L.; Zheng, B.; Yuan, H.; Xie, S.; Xiao, D.; Choi, M. Microwave-assisted non-aqueous homogeneous precipitation of nanoball-like mesoporous α-$Ni(OH)_2$ as a precursor for niox and its application as a pseudocapacitor. *J. Mater. Chem.* **2012**, *22*, No. 8029.
(22) Farhadi, S.; Pourzare, K.; Bazgir, S. Co_3O_4 nanoplates: synthesis, characterization and study of optical and magnetic properties. *J. Alloys Compd.* **2014**, *587*, 632−637.
(23) Zhong, M.; Hisatomi, T.; Kuang, Y.; Zhao, J.; Liu, M.; Iwase, A.; Jia, Q.; Nishiyama, H.; Minegishi, T.; Nakabayashi, M.; Shibata, N.; Niishiro, R.; Katayama, C.; Shibano, H.; Katayama, M.; Kudo, A.; Yamada, T.; Domen, K. Surface modification of CoO_x loaded bivo4 photoanodes with ultrathin p-type NiO layers for improved solar water oxidation. *J. Am. Chem. Soc.* **2015**, *137*, 5053−5060.
(24) Pan, B.; Meng, X.; Xia, Y.; Lu, H.; Li, H. Raman shift, néel temperature, and optical band gap of NiO nanoparticles. *Phys. Chem. Chem. Phys.* **2020**, *22*, 5735−5739.
(25) Ijaz, I.; Gilani, E.; Nazir, A.; Bukhari, A. Detail review on chemical, physical and green synthesis, classification, characterizations and applications of nanoparticles. *Green Chem. Lett. Rev.* **2020**, *13*, 223−245.
(26) Newville, M.; Līviņš, P.; Yacoby, Y.; Rehr, J.; Stern, E. Near-edge x-ray-absorption fine structure of pb: a comparison of theory and experiment. *Phys. Rev. B* **1993**, *47*, 14126−14131.
(27) Ganguli, T.; Sinha, A.; Narayana, C.; Upadhyay, A.; Singh, M.; Saxena, P.; Dubey, V.; Singh, I.; Raja, S.; Vora, H.; Deb, S. A high pressure XRD setup at ADXRD beamline (BL-12) on Indus-2. *J. Phys.: Conf. Ser.* **2013**, *425*, No. 112001.
(28) Poswal, A.; Agrawal, A.; Poswal, H.; Bhattacharyya, D.; Jha, S.; Sahoo, N. Augmentation of the step-by-step energy-scanning EXAFS beamline BL-09 to continuous-scan EXAFS mode at INDUS-2 SRS. *J. Synchrotron Radiat.* **2016**, *23*, 1518−1525.
(29) Basu, S.; Nayak, C.; Yadav, A.; Agrawal, A.; Poswal, A.; Bhattacharyya, D.; Jha, S.; Sahoo, N. A comprehensive facility for EXAFS measurements at the INDUS-2 synchrotron source at RRCAT, Indore, India. *J. Phys.: Conf. Ser.* **2014**, *493*, No. 012032.
(30) Sinha, A.; Sagdeo, A.; Gupta, P.; Upadhyay, A.; Kumar, A.; Singh, M.; Gupta, R.; Kane, S.; Verma, A.; Deb, S. Angle dispersive X-ray diffraction beamline on Indus-2 synchrotron radiation source: commissioning and first results. *J. Phys.: Conf. Ser.* **2013**, *425*, No. 072017.
(31) Rodríguez-Carvajal, J. Recent Advances in Magnetic Structure Determination by Neutron Powder Diffraction. *Phys. B* **1993**, *192*, 55−69.
(32) Wu, Z.; Huang, X.; Wang, Z.; Xu, J.; Wang, H.; Zhang, X. Electrostatic induced stretch growth of homogeneous β -Ni(OH)2 on graphene with enhanced high-rate cycling for supercapacitors. *Sci. Rep.* **2014**, *4*, No. 3669.
(33) Gawali, S.; Gandhi, A.; Gaikwad, S.; Pant, J.; Chan, T.; Cheng, C.; Ma, Y.; Wu, S. Role of cobalt cations in short range antiferromagnetic Co_3O_4 nanoparticles: a thermal treatment approach to affecting phonon and magnetic properties. *Sci. Rep.* **2018**, *8*, No. 249.
(34) Wu, S.; Ji, J.; Chou, M.; Li, W.; Chi, G. Low-temperature phase separation in gan nanowires: an in situ X-ray investigation. *Appl. Phys. Lett.* **2008**, *92*, No. 161901.
(35) Kizler, P. X-ray-absorption near-edge structure spectra for bulk materials: multiple-scattering analysis versus a phenomenological approach. *Phys. Rev. B* **1992**, *46*, 10540−10546.
(36) Kuzmin, A.; Mironova, N.; Purans, J.; Rodionov, A. X-Ray absorption spectroscopy study of Nicmg1-Co solid solutions on the Ni K Edge. *J. Condens. Matter Phys.* **1995**, *7*, 9357−9368.
(37) Baumgartel, H. *EXAFS, SEXAFS, XANES: X-Ray Absorption—Principles, Applications, Techniques of EXAFS, SEXAFS and XANES*, InVon Koningsberger, D.; Prins, R., Eds.; John Wiley & Sons Ltd.: Chichester, 1988; p 673.
(38) Newville, M.; Ravel, B.; Haskel, D.; Rehr, J.; Stern, E.; Yacoby, Y. Analysis of multiple-scattering XAFS data using theoretical standards. *Phys. B: Condens. Matter* **1995**, *208−209*, 154−156.
(39) Bergmann, A.; Martinez-Moreno, E.; Teschner, D.; Chernev, P.; Gliech, M.; de Araújo, J.; Reier, T.; Dau, H.; Strasser, P. Reversible amorphization and the catalytically active state of crystalline Co_3O_4 during oxygen evolution. *Nat. Commun.* **2015**, *6*, No. 8625.
(40) Haider, A.; Ijaz, M.; Ali, S.; Haider, J.; Imran, M.; Majeed, H.; Shahzadi, I.; Ali, M.; Khan, J.; Ikram, M. Green synthesized phytochemically (zingiber officinale and allium sativum) reduced Nickel Oxide nanoparticles confirmed bactericidal and catalytic potential. *Nanoscale Res. Lett.* **2020**, *15*, No. 50.
(41) Moavi, J.; Buazar, F.; Sayahi, M. Algal magnetic Nickel Oxide nanocatalyst in accelerated synthesis of pyridopyrimidine derivatives. *Sci. Rep.* **2021**, *11*, No. 6296.
(42) Ma, W.; Wang, L.; Xue, J.; Cui, H. A bottom-up strategy for exfoliation-free synthesis of soluble α-$Ni(OH)_2$ monolayer nanosheets on a large scale. *RSC Adv.* **2016**, *6*, 85367−85373.
(43) Diallo, A.; Beye, A.; Doyle, T.; Park, E.; Maaza, M. Green synthesis of Co_3O_4 nanoparticles viaaspalathus linearis: physical properties. *Green Chem. Lett. Rev.* **2015**, *8*, 30−36.
(44) Hall, D.; Lockwood, D.; Poirier, S.; Bock, C.; MacDougall, B. Applications of in situ Raman spectroscopy for identifying nickel hydroxide materials and surface layers during chemical aging. *ACS Appl. Mater. Interfaces* **2014**, *6*, 3141−3149.
(45) Zhao, Y.; Chen, S.; Sun, B.; Su, D.; Huang, X.; Liu, H.; Yan, Y.; Sun, K.; Wang, G. Graphene-Co_3O_4 nanocomposite as electrocatalyst with high performance for oxygen evolution reaction. *Sci. Rep.* **2015**, *5*, No. 7629.
(46) Cho, S.; Jung, J.; Kim, C.; Kim, I. Rational Design of 1-D Co_3O_4 Nanofibers@Low Content Graphene Composite Anode for High Performance Li-Ion Batteries. *Sci. Rep.* **2017**, *7*, No. 45105.
(47) Saykar, N.; Pilania, R.; Banerjee, I.; Mahapatra, S. Synthesis of NiO-Co_3O_4 Nanosheet and Its Temperature-Dependent Super-capacitive Behavior. *J. Phys. D: Appl. Phys.* **2018**, *51*, No. 475501.
(48) Wang, J.; Uma, S.; Klabunde, K. Visible light photocatalytic activities of transition metal oxide/silica aerogels. *Microporous Mesoporous Mater.* **2004**, *75*, 143−147.
(49) Katsoulidis, A.; Petrakis, D.; Armatas, G.; Trikalitis, P.; Pomonis, P. Ordered mesoporous CoO_x/MCM-41 materials exhibiting long-range self-organized nanostructured morphology. *Microporous Mesoporous Mater.* **2006**, *92*, 71−80.
(50) Feng, C.; Wang, H.; Zhang, J.; Hu, W.; Zou, Z.; Deng, Y. One-pot facile synthesis of Cobalt Oxide nanocubes and their magnetic properties. *J. Nanopart. Res.* **2014**, *16*, No. 2413.
(51) Baig, U.; Khan, A.; Gondal, M.; Dastageer, M.; Falath, W. Laser induced anchoring of Nickel Oxide nanoparticles on polymeric graphitic carbon nitride sheets using pulsed laser ablation for efficient water splitting under visible light. *Nanomaterials* **2020**, *10*, No. 1098.
(52) Neiva, E.; Oliveira, M.; Bergamini, M.; Marcolino, L.; Zarbin, A. One material, multiple functions: graphene/$Ni(OH)_2$ thin films applied in batteries, electrochromism and sensors. *Sci. Rep.* **2016**, *6*, No. 33806.
(53) TaghaviMoghadam, J.; Knowles, G.; Chaffee, A. SBA-15 supported cobalt oxide species: synthesis, morphology and catalytic oxidation of cyclohexanol using TBHP. *J. Mol. Catal. A Chem.* **2013**, *379*, 277−286.

https://doi.org/10.1021/acsomega.1c06179
ACS Omega 2022, 7, 6700−6709